



Contents lists available at ScienceDirect

# International Journal of Pressure Vessels and Piping

journal homepage: [www.elsevier.com/locate/ijpvp](http://www.elsevier.com/locate/ijpvp)



## T-stress solutions for through-wall circumferential cracks in straight pipes under bending



M. Gintalas<sup>a,\*</sup>, R.A. Ainsworth<sup>b</sup>, F. Scenini<sup>c</sup>

<sup>a</sup> The University of Cambridge, Department of Materials Science and Metallurgy, Maxwell Centre, JJ Thomson Ave, Cambridge, CB3 0HE, UK

<sup>b</sup> The University of Manchester, School of Mechanical, Aerospace and Civil Engineering, Pariser Building, Sackville Street, Manchester M13 9PL, UK

<sup>c</sup> The University of Manchester, School of Materials, Sackville Street, Manchester M13 9PL, UK

### ARTICLE INFO

#### Article history:

Received 14 December 2016

Received in revised form

2 April 2017

Accepted 20 April 2017

Available online 22 April 2017

#### Keywords:

T-stress

Crack

Pipe

### ABSTRACT

This paper reports the results of an extensive series of finite element calculations to provide normalised T-stress solutions for through-wall cracked pipes under bending for a range of crack sizes and pipe radius to wall thickness ratios. Comparisons with the limited solutions in the literature are used to give confidence in the numerical solutions obtained, which are shown to be sensitive to mesh refinement. The results are provided in a form that is suitable for use in practical constraint based defect assessment approaches.

© 2017 Elsevier Ltd. Open access under [CC BY](https://creativecommons.org/licenses/by/4.0/) license.

### 1. Introduction

The fracture toughness of a material generally depends on the structural thickness, nature of the loading, relative crack size and crack-tip constraint [1]. However, these dependencies are disregarded for many engineering purposes and the plane strain fracture toughness, measured using deeply cracked standard bend specimens, is often used as a material property because it leads to the most conservative fracture assessments. Where cracks are small, for instance in pipes in the oil and gas industry and in nuclear power plant, this approach can be overly conservative because the constraint levels at the crack-tip are lower than those in standard cracked bend specimens. While full-scale pipe tests could be used to avoid introduction of this conservatism, this would require custom testing facilities and high testing costs. A more attractive option is to find a small-scale cracked specimen geometry which has a crack-tip constraint level similar to that in a large-scale cracked pipe. For example, low constraint levels and corresponding higher toughness values can be obtained by testing Single Edge Notch Bend (SENB) specimens with shallow cracks [2].

New designs of fracture toughness test specimen, such as curved compact tension specimens and compact pipe tension specimens

[3,4], which would ensure similar or even the same constraint level at the crack-tip as cracked pipes, have been investigated. This has led to the application of Single Edge Notch Tension (SENT) specimens in the offshore industry, as this type of specimen has been shown to adequately reproduce the stress and strain fields in a pipe for a range of loadings [2,5]. In particular, it was found that the crack-tip constraint of a SENT specimen is close to that of an axially cracked pipe [6,7]. Additionally, it has been found that the fracture toughness obtained from low constraint SENT and shallow-notched SENB specimens is appropriate for the assessment of circumferential flaws in pipes [8]. Analysis based on SENT and SENB specimens showed that an approach based on quantifying constraint using the elastic T-stress could be used not only to estimate initiation fracture toughness but also to develop constraint-corrected resistance curves [8]. In fact, T-stress has been considered successfully for resistance curve modelling by Nyhus et al. [9]. It has been shown that the ductile crack resistance curves can be normalised not only by  $Q$  but also by the T stress. This finding implies that the T stress influences ductile fracture.

To apply elastic constraint based failure assessment methods to cracked structural analysis, the stress intensity factor,  $K_I$ , may be paired with the T-stress. Such two parameter approaches may be used to apply material fracture toughness from small-scale laboratory specimens to fracture in large-scale components [10]. A constraint-based fracture mechanics methodology based on a two-parameter  $K_I - T$  characterization of the crack-tip fields has been

\* Corresponding author.

E-mail address: [mg793@cam.ac.uk](mailto:mg793@cam.ac.uk) (M. Gintalas).

employed for constraint assessments in specimens and pipes [7].

To apply  $K_I - T$  approaches, solutions for  $K_I$  and  $T$  for practical cracked geometries are required. While solutions for  $K_I$  are widely available,  $T$ -stress solutions are limited although compendia of these limited solutions are contained in failure assessment codes such as R6 [10]. Huh [11], Jayadevan et al. [12], Qian [13] and Lewis

$$T = (\sigma_{xx} - \sigma_{yy})_{r \rightarrow 0, \varphi=0} \quad (2)$$

is the constant stress acting parallel to the crack flank in the near-tip elastic stress field.

From Eq. (1), the in-plane principal stresses,  $\sigma_1, \sigma_2$ , and in plane strain, the third principal stress,  $\sigma_3$ , are [15]

$$\begin{aligned} \sigma_1 &= \frac{1}{4} \left\{ 2T + \frac{4K_I}{\sqrt{2\pi r}} \cos\left(\frac{\varphi}{2}\right) + \sqrt{2 \left[ \left( \frac{K_I}{\sqrt{2\pi r}} \right)^2 (1 - \cos(2\varphi)) + 2T^2 + 2T \frac{K_I}{\sqrt{2\pi r}} \left( \cos\left(\frac{5\varphi}{2}\right) - \cos\left(\frac{\varphi}{2}\right) \right) \right]} \right\} \\ \sigma_2 &= \frac{1}{4} \left\{ 2T + \frac{4K_I}{\sqrt{2\pi r}} \cos\left(\frac{\varphi}{2}\right) - \sqrt{2 \left[ \left( \frac{K_I}{\sqrt{2\pi r}} \right)^2 (1 - \cos(2\varphi)) + 2T^2 + 2T \frac{K_I}{\sqrt{2\pi r}} \left( \cos\left(\frac{5\varphi}{2}\right) - \cos\left(\frac{\varphi}{2}\right) \right) \right]} \right\} \\ \sigma_3 &= \nu \left[ T + \frac{2K_I}{\sqrt{2\pi r}} \cos\left(\frac{\varphi}{2}\right) \right] \end{aligned} \quad (3)$$

and Wang [14] have performed  $T$ -stress analysis in pipes with circumferential cracks. However, most of these solutions are for part-through-wall defects and only the work of Lewis and Wang [14] deals with circumferential through-wall cracks in pipes.

This paper presents elastic finite element studies for  $T$ -stress and stress intensity factor solutions for circumferentially through-wall cracked pipes using three-dimensional solid elements. Firstly, Section 2 provides some background to the  $T$ -stress and the normalisation used in the paper. Then, Section 3 presents the pipe geometry and loading considered. It was found that the results obtained were sensitive to mesh refinement using solid elements and therefore Section 4 describes a detailed mesh refinement study for a SENB specimen, for which well-established solutions are available for comparison. Section 5 presents the pipe solutions using refined shell and solid element meshes and compares these with the solutions obtained by Lewis and Wang [14] using shell elements. Finally, the discussion of the results and the conclusions are reported in Sections 6 and 7 respectively.

## 2. The elastic $T$ -stress

The stress intensity factor,  $K_I$ , and the  $T$ -stress characterize the elastic crack-tip stress and strain fields. Both  $K_I$  and  $T$  are directly proportional to the load applied to a cracked geometry and the crack-tip stress field is defined by

$$\begin{Bmatrix} \sigma_{xx} \\ \sigma_{yy} \\ \tau_{xy} \end{Bmatrix} = \frac{K_I}{\sqrt{2\pi r}} \cos\left(\frac{\varphi}{2}\right) \begin{Bmatrix} 1 - \sin\left(\frac{\varphi}{2}\right) \sin\left(\frac{3\varphi}{2}\right) \\ 1 + \sin\left(\frac{\varphi}{2}\right) \sin\left(\frac{3\varphi}{2}\right) \\ \sin\left(\frac{\varphi}{2}\right) \cos\left(\frac{3\varphi}{2}\right) \end{Bmatrix} + \begin{Bmatrix} T \\ 0 \\ 0 \end{Bmatrix} \quad (1)$$

where  $\sigma_{xx}, \sigma_{yy}, \tau_{xy}$  are the normal and shear stress components,  $K_I$  is the opening mode stress intensity factor,  $r$  is distance from the crack-tip and  $\varphi$  is the polar angle measured from the  $x$ -axis. Then,

where  $\nu$  is Poisson's ratio. The effect of the  $T$ -stress on the hydrostatic stress,  $\sigma_m$ , is then:

$$\sigma_m = \frac{\sigma_1 + \sigma_2 + \sigma_3}{3} = \frac{1}{3}(1 - \nu) \left[ T + 2 \frac{K_I}{\sqrt{2\pi r}} \cos\left(\frac{\varphi}{2}\right) \right] \quad (4)$$

Eq. (4) shows that a negative  $T$ -stress decreases the hydrostatic stress level and positive  $T$  values increases the hydrostatic stress. This is referred to as positive  $T$ -stress increasing the level of crack-tip stress triaxiality and leading to high crack-tip constraint, whilst negative  $T$ -stress reduces the level of crack-tip stress triaxiality and leads to low crack-tip constraint [16]. A loss of constraint in specimens leads to an increase in the measured fracture toughness. This can be explained by increased hydrostatic stress reducing the driving force for dislocation emission and plasticity generation, as demonstrated via continuum predictions and atomistic simulations, and therefore the material behaving in a more brittle manner [17] under high constraint conditions. The  $T$ -stress may also influence the crack growth path and in general, if  $T < 0$ , the crack propagation path follows a straight line and for  $T > 0$  it follows a curve [1,18,19]. The  $T$ -stress can also be used to characterise constraint levels in 3D cracked bodies [20] and also used to predict the potential propagation path of longitudinal and circumferential defects in pressure vessels [21].

When performing fracture mechanics assessments, elastic analysis is often not adequate and allowance needs to be made for plasticity. In defect assessment procedures such as R6 [10], plasticity is accounted for using a plastic collapse parameter  $L_r$ , which is the ratio of the applied load to the plastic collapse load, defined using the yield stress  $\sigma_y$ . The ratio of the  $T$ -stress to the yield stress  $\sigma_y$  of the material is also important and since both  $T$  and  $L_r$  are directly proportional to load, the R6 procedure [10] quantifies constraint using a normalised constraint parameter  $\beta_T$ :

$$\beta_T L_r = T/\sigma_y \quad (5)$$

which is independent of both load magnitude and material properties. Results for  $T$ -stress in this paper are presented in terms of this non-dimensional parameter and low constraint geometries/

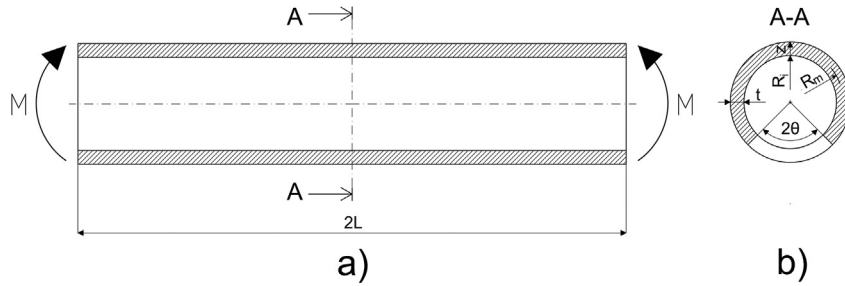


Fig. 1. a) pipe under pure bending moment M, b) pipe cross-section.

loadings correspond to negative values of  $\beta_T$ .

### 3. Geometry and loading of cracked pipe

The pipe analysed in this study is shown in Fig. 1. A range of ratios of wall thickness,  $t$ , to mean radius,  $R_m$ , is considered as well as a range of crack circumferential crack length  $2a = 2R_m\theta$ . The pipe is of total length,  $2L$ , and is subjected to a pure bending moment,  $M$ , which induces a complex stress state in a cracked pipe.

For the cases considered, there are solutions available in the literature for plastic collapse moment, stress intensity factor and T-stress, as summarised here. The R6 compendium [10] contains collapse load solutions for cracked pipes subjected to combined bending moment, internal pressure and end-force which were derived from the work of Lei et al. [22]. For pure bending the solution simplifies to:

$$M_L^{pipe} = 4R_m^2\sigma_y[\cos(\theta/2) - (1/2)\sin\theta][1 + (1/12)(t/R_m)^2] \quad (6)$$

The normalized stress intensity factor,  $F_b = K_I/(\sigma_b(\pi a)^{0.5})$ , where the nominal bending stress is  $\sigma_b = M/(\pi t(R_m)^2)$ , is used for comparison purposes later in the paper and the reference solution is taken from Lacire et al. [23] and is:

$$F_b = [1 + (t/2R_m)] [A_b + B_b(\theta/\pi) + C_b(\theta/\pi)^2 + D_b(\theta/\pi)^3 + E_b(\theta/\pi)^4] \quad (7)$$

$$A_b = 0.65133 - 0.5774\eta - 0.3427\eta^2 - 0.0681\eta^3 \quad B_b = 1.879 + 4.795\eta + 2.343\eta^2 - 0.6197\eta^3$$

$$C_b = -9.779 - 38.14\eta - 6.611\eta^2 + 3.972\eta^3 \quad D_b = 34.56 + 129.9\eta + 50.55\eta^2 + 3.374\eta^3$$

$$E_b = -30.82 - 147.6\eta - 78.38\eta^2 - 15.54\eta^3 \quad \eta = \log(t/R_m)$$

A normalized T-stress solution for circumferential through-wall cracked pipes has been derived by Lewis and Wang [14] using re-sults finite element models using shell elements:

Table 1  
Coefficients in Eq. (9) from Lewis and Wang [14].

i	Constraint Coefficient		
	$C_{i0}$	$C_{i1}$	$C_{i2}$
1	-0.934	-0.01	0.0005
2	4.3575	1.2671	-0.0451
3	74.273	-35.312	0.9889
4	-680.39	266.98	-6.3389
5	2688.6	-957.82	20.135
6	-3852.8	1325	-25.744

$$T/\sigma_b = C_1 + C_2(\theta/\pi)^2 + C_3(\theta/\pi)^4 + C_4(\theta/\pi)^6 + C_5(\theta/\pi)^8 + C_6(\theta/\pi)^{10} \quad (8)$$

The coefficients  $C_i(i = 1-6)$  in Eq. (8) are functions of the mean radius to thickness ratio  $R_m/t$ :

$$C_i = C_{i0} + C_{i1}(R_m/t) + C_{i2}(R_m/t)^2 \quad (9)$$

where the coefficients  $C_{ij}$  from [14] are given in Table 1.

This solution is used with Eq. (6) to give the normalised T-stress of Eq. (5) for comparison with the solutions presented from the current analyses using solid 3D finite element modelling.

### 4. Analysis of mesh refinement in the SENB specimen

Preliminary analyses of the cracked pipe geometry of Section 3 indicated that the results were sensitive to mesh refinement using solid elements. Therefore, a detailed mesh refinement study was undertaken for a SENB specimen, for which there are well-established solutions for the limit load, stress intensity factor and T-stress. The geometry and loading for the SENB specimen are shown in Fig. 2.

The limit load,  $P_L$ , for the SENB specimen is expressed as [10]:

$$P_L = (W^2B\sigma_y/S)p_L \quad (10)$$

where  $W$ ,  $B$  and  $S$  are the specimen width, thickness and span and  $p_L$  for the plane strain von Mises yield criterion is:

$$p_L = \begin{cases} \frac{2}{\sqrt{3}}(1.12 + 1.13\alpha - 3.194\alpha^2)(1 - \alpha)^2 & 0 \leq \alpha \leq 0.18 \\ \frac{2.44}{\sqrt{3}}(1 - \alpha)^2 & 0.18 < \alpha < 1.0 \end{cases} \quad (11)$$

where  $\alpha$  is the relative crack depth,  $a/W$ . The stress intensity factor is [10]:

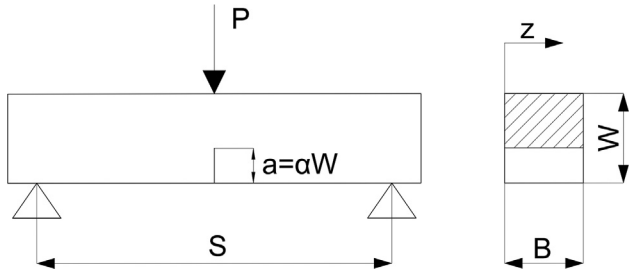


Fig. 2. SENB specimen loaded under three-point bending.

$$K_I = \frac{3FS}{2BW^{1.5}} F_b \quad (12)$$

where  $P$  is the applied load and the function  $F_b$  for  $S/W = 4$  is:

$$F_b = \sqrt{\alpha} \frac{1.99 - (\alpha)(1 - \alpha)[2.15 - 3.93\alpha + 2.7\alpha^2]}{(1 + 2\alpha)(1 - \alpha)^{1.5}} \quad (13)$$

The accuracy of Eq. (13) is quoted in the source reference [10] as within 0.5% for any  $\alpha$ .

Values of the constraint parameter  $\beta_T$  of Eq. (5) with  $L_r = P/P_L$  were calculated using the solutions above and the T-stress in [10]. The plane strain value of  $\beta_T$  for  $S/W = 4$ , valid for  $0 \leq \alpha \leq 0.8$ , is:

$$\beta_T = -0.9893 + 4.8784(\alpha) - 9.6956(\alpha)^2 + 11.434(\alpha)^3 - 5.9061(\alpha)^4 \quad (14)$$

The remainder of this section reports 3D elastic finite element studies to determine the mesh refinement necessary to accurately reproduce the elastic solutions of Eq. (12) and (14).

#### 4.1. Mesh refinement

The SENB specimen was modelled using ABAQUS 6.14 [24], with a focussed mesh consisting of 20 rings of elements surrounding the crack-tip and a more coarse mesh elsewhere. A typical mesh is shown in Fig. 3. The crack-tip was enclosed by a ring of full integration wedge type C3D15 (9 integration points) elements. For the remainder of the model, eight node full integration elements, C3D8, were found to be adequate for stress intensity factor calculations but not for T-stress analysis, while reduced, C3D20R integration elements led to oscillation in the stress results. The highest element

order element, C3D20 (27 integration points), available through the ABAQUS graphical user interface, was therefore used for all 3D analyses. Only half of the specimen subjected to  $P = 1000$  N was modelled due to symmetry conditions. Stress intensity factor and T stress values were also extracted at  $P = 1000$  N. Within ABAQUS the T-stress extraction based on an interaction integral technique [24,25] is included in the graphical user interface.

The mesh was refined by varying the number of elements in the rings surrounding the crack-tip and the size of the focussed mesh region, Fig. 3(b), the element densities outside the focussed mesh,  $N_{W-a}$  and  $N_{S/2}$ , along the specimen remaining ligament of length  $W-a$  and semi-span of length  $S/2$ , respectively, Fig. 3(a), and the number of elements through the section thickness. Unless, specified otherwise, results presented below are those at the specimen mid-plane; variations through the thickness are discussed in Section 4.2.

Mesh independence for  $F_b$  and  $\beta_T$  was achieved when there were 16 elements in each ring surrounding the crack-tip, although the T-stress was found to be more sensitive to mesh refinement than the stress intensity factor, for which convergence could be obtained with a smaller number of elements. Rings of 16 elements were therefore used in subsequent mesh refinement studies.

The influence of the element densities,  $N_{W-a}$  and  $N_{S/2}$ , along the specimen remaining ligament of length  $W-a$  and semi-span of length  $S/2$ , respectively, was also examined. The mesh in Fig. 3 has  $N_{W-a} = 7$  and  $N_{S/2} = 19$ . The dependencies on mesh numbers are summarised in Figs. 4 and 5, where the stress intensity factor and T-stress have been evaluated on the contours surrounding the 20 rings of elements at the crack-tip. The far field mesh has little effect on the stress intensity factor solution unless the mesh is very coarse but does affect the T-stress solution. Convergence was achieved at  $N_{W-a} = 7$  and  $N_{S/2} = 19$ , which leads to elements with square in-plane dimensions.

#### 4.2. Comparisons with handbook solutions and effect of thickness

It has been shown above that converged solutions can be obtained with increasing mesh refinement but it is also necessary to demonstrate that the solutions converge to the correct values. Therefore, Fig. 5 includes solutions from R6 [10] for  $F_b$ , Fig. 5(a), and  $\beta_T$ , Fig. 5(b). As the R6 solutions are for plane strain, this condition has been simulated by applying boundary conditions on the specimen side surfaces which suppress movement along the thickness direction.

It can be seen from Fig. 5 that the finite element results from the

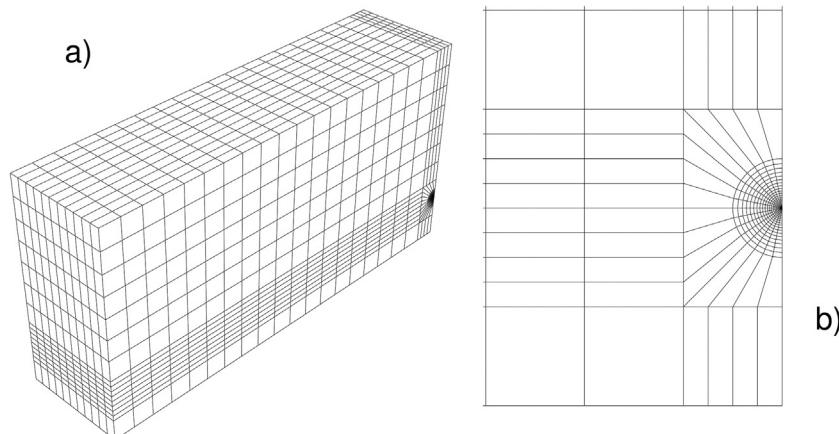


Fig. 3. Typical SENB mesh showing a) overall geometry and b) section around the crack-tip.

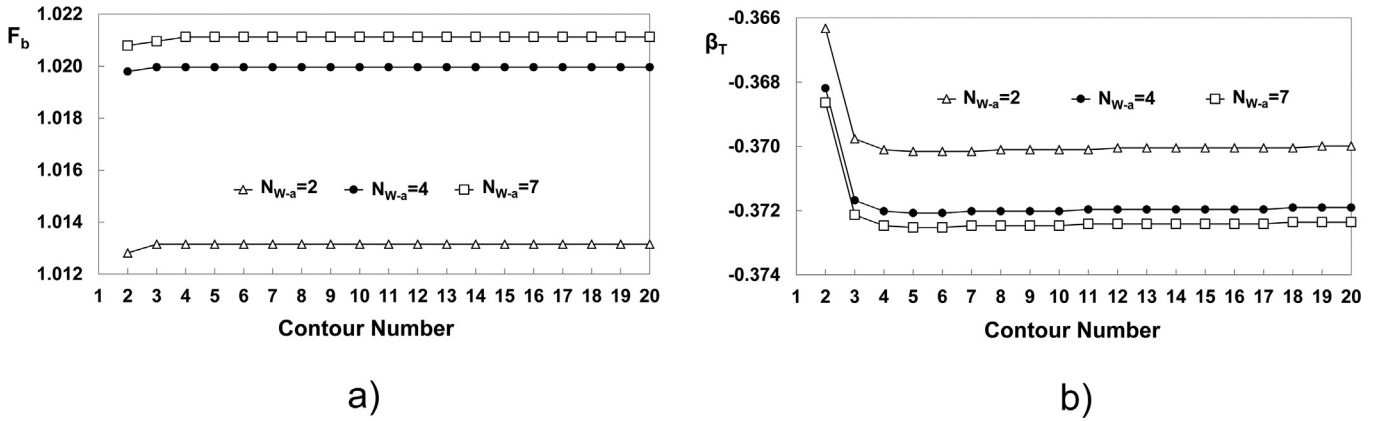


Fig. 4. Influence of element number  $N_{W-a}$  along remaining ligament, with number of elements along semi-span fixed at  $N_{S/2} = 3$ , on a) the normalised stress intensity  $F_b$  and b) the normalised T-stress,  $\beta_T$ .

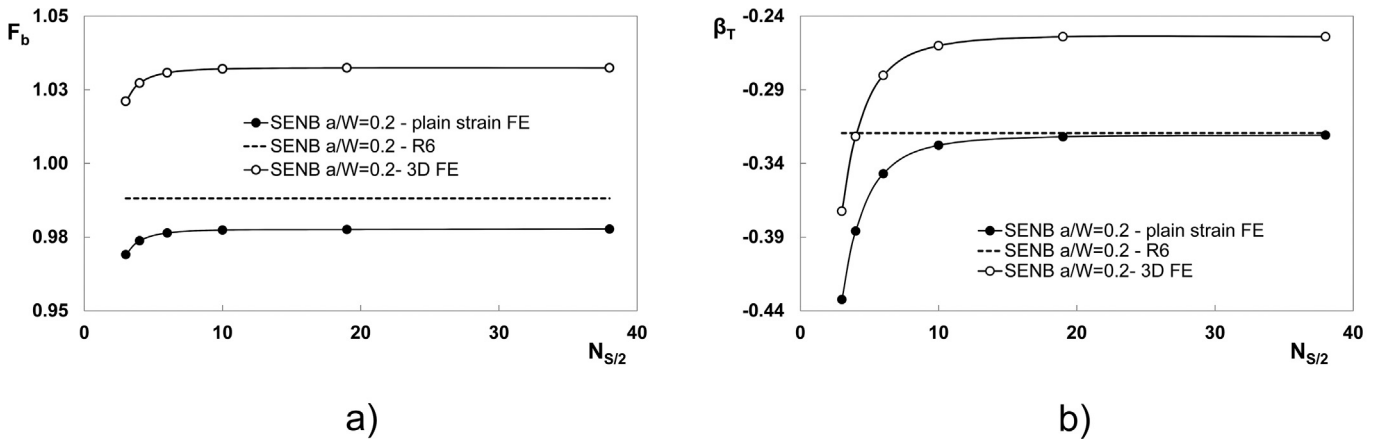


Fig. 5. Influence of element number  $N_{S/2}$  along semi-span, with number of elements along remaining ligament fixed at  $N_{W-a} = 7$  on a) the normalised stress intensity  $F_b$  and b) the normalised T-stress,  $\beta_T$ . Comparisons with R6 solutions [10] are also shown.

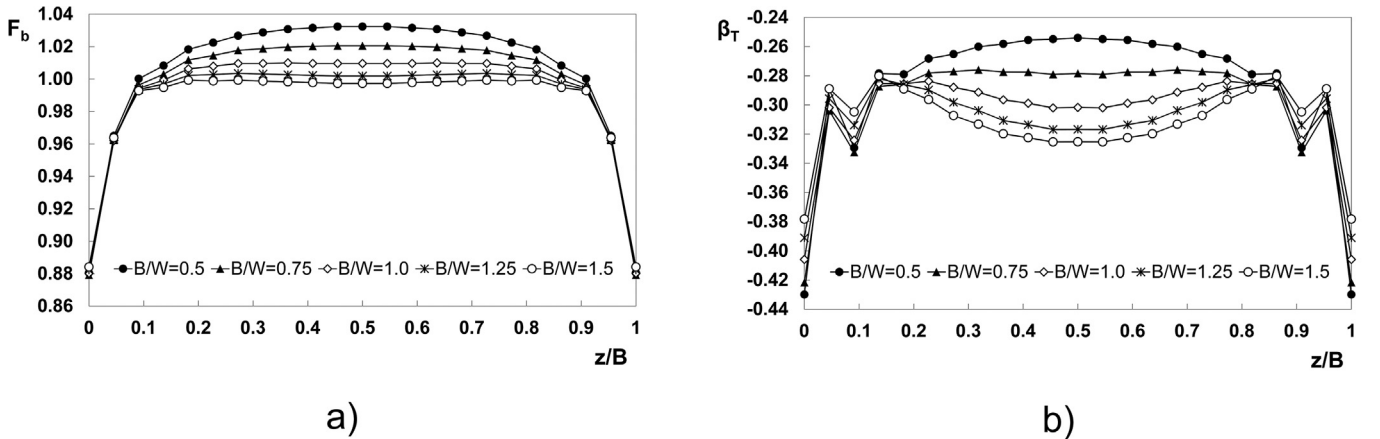


Fig. 6. Through thickness variations of a) the normalised stress intensity  $F_b$  and b) the normalised T-stress,  $\beta_T$  for a range of  $B/W$ .

plane strain model are very close to the R6 solutions. However, the results from the 3D model, without imposing constraints on the side surfaces, show that there is an influence of specimen thickness on both  $F_b$  and  $\beta_T$  compared with the idealised plane strain case, and this is examined next.

In order to examine the influence of specimen thickness,

simulations were performed with  $B/W = 0.5, 0.75, 1.0, 1.25$  and  $1.5$ , initially with the number of elements through the thickness,  $N_B$ , fixed at  $N_B = 11$  for all values of  $B/W$ . The geometry in Fig. 3 is  $B/W = 0.5$ . Fig. 6 shows a significant effect of  $B/W$  on  $\beta_T$  at the mid-plane,  $z = B/2$ , whereas  $F_b$  at the mid-plane only varies by about 3% between all the cases considered. This demonstrates that the

**Table 2**  
Normalised mid-plane T-stress for three-point-bend specimens from [26] and current study.

a/W	B/W							Normalisation	Ref.
	0.1	0.25	0.5	1	1.5	2	40		
0.2	-0.158	-0.182	-0.188	-0.22	-0.236	-0.240	-0.244	$T(\pi a)^{1/2}/K_I$	[26]
	-0.211	-0.243	-0.251	-0.294	-0.315	–	–	Eq. (5)	[26]
	-0.213	-0.246	-0.254	-0.302	-0.325	–	–	Eq. (5)	Current study

normalised stress intensity factor is less sensitive to geometry than the normalised constraint parameter.

The trends in Fig. 6 are similar to those from the literature [26] where 3D T-stress solutions were obtained by running finite element analyses for three-point-bend specimens with wide ranges of crack depth to specimen width ratio ( $a/W = 0.2–0.8$ ) and specimen thickness to width ratio ( $B/W = 0.1–40$ ). The results from [26] for  $a/W = 0.2$ , normalised as  $T(\pi a)^{1/2}/K_I$ , are presented in Table 2 and show reducing constraint with increasing B/W, approaching a limiting value for large B/W. The current results in Fig. 6 show the same trends. With increase of B/W, the stress state at the mid-plane approaches plane strain and hence the normalised T-stress in Fig. 6 approaches the plane strain solution shown in Fig. 5(b).

The influence of the number of elements through the specimen thickness ( $N_B = 11, 22, 33$ ) was also examined. Although the mesh density was found to affect the T-stress solution in the most outer element layers, where due to free surface effects it is difficult to judge the reliability of values obtained, the results for different values of  $N_B$  were found to be indistinguishable in the central part of the specimen ( $0.14 < z/B < 0.86$ ). Stress intensity factor solutions were found to be independent of  $N_B$  over the whole of the specimen thickness.

## 5. Solutions for through-wall cracked pipes

### 5.1. Finite element model of cracked pipe using shell elements

Stress distributions in pipes can be simulated using shell elements [14,23], which require significantly less computational power compared to 3D solid elements. Therefore, the use of shell elements is an attractive option for parametric studies to obtain T-stress solutions in pipes. A cracked pipe finite element model was created using shell elements for a quarter pipe with  $R_m/t = 5$  and  $\theta/\pi$  in the range 0.05–0.5. The model was subjected to a pure bending moment of  $5 \cdot 10^4$  Nmm at which T and K values were extracted. The meshing experience obtained with the SENB study was applied to

the cracked pipe. A focused mesh at the crack-tip identical to that in the SENB specimen in terms of configuration and element shape was used in the cracked pipe study.

The pipe length, L, was chosen equal to 100 mm and the radius  $R_m = 11$  mm for all cases analysed. Around the semi-circumference of the cylinder, the mesh contained 34 elements resulting in an element size of edge = 1 mm, consistent with the element size along the ligament from the SENB study when  $N_{W-a} = 7$ . The number of elements along the pipe length was chosen as 100, leading to square elements in the far field, again in agreement with the SENB experience. A typical mesh is shown in Fig. 7.

The stress intensity factor and T-stress results from the current FE study are compared with the solutions of Lacire et al. [23] and Lewis and Wang [14], respectively, in Fig. 8.

It can be seen that the current shell element study using the meshing technique developed for the SENB specimen replicates the normalized stress intensity factor results of Lacire et al. [23] and the T-stress solutions of Lewis and Wang [14].

### 5.2. Finite element model of cracked pipe using 3D solid elements

The meshing technique developed in Section 4 was also used to model the cracked pipe model with 3D solid elements. Again, the focused mesh area at the crack-tip was identical to that in the converged SENB model in terms of configuration and elements shape. As in Section 5.1, a quarter pipe model was subjected to a pure bending moment of  $5 \cdot 10^4$  Nmm at which T and K values were extracted.

The finite element models contained 11 elements through the thickness. This gives 12 layers of nodes located on an element edge plane and 11 layers of nodes located on element mid-planes. Therefore, there are 23 layers of nodes through the thickness. Since T-stress estimation is inaccurate in regions close to where a crack intersects a free surface [18], only results from node layers numbered from 5 to 19 were used and these correspond to normalised positions  $z/t = 0.18$  and  $z/t = 0.82$ , respectively, through the pipe thickness (Fig. 1).

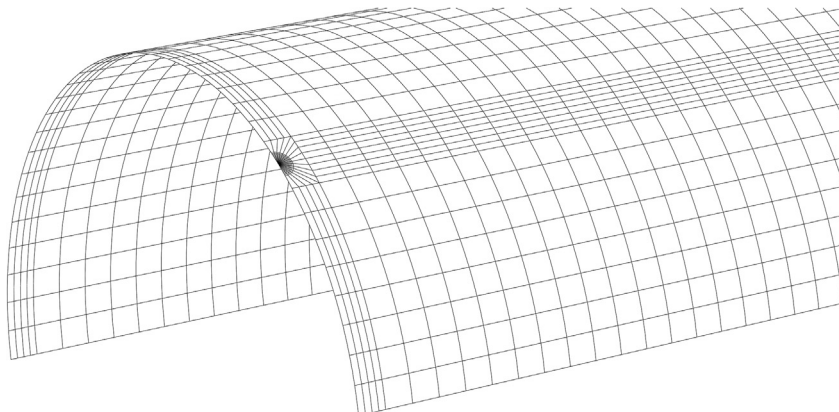


Fig. 7. Shell element mesh for circumferential through-wall cracked pipe with  $\theta/\pi = 0.25$ .

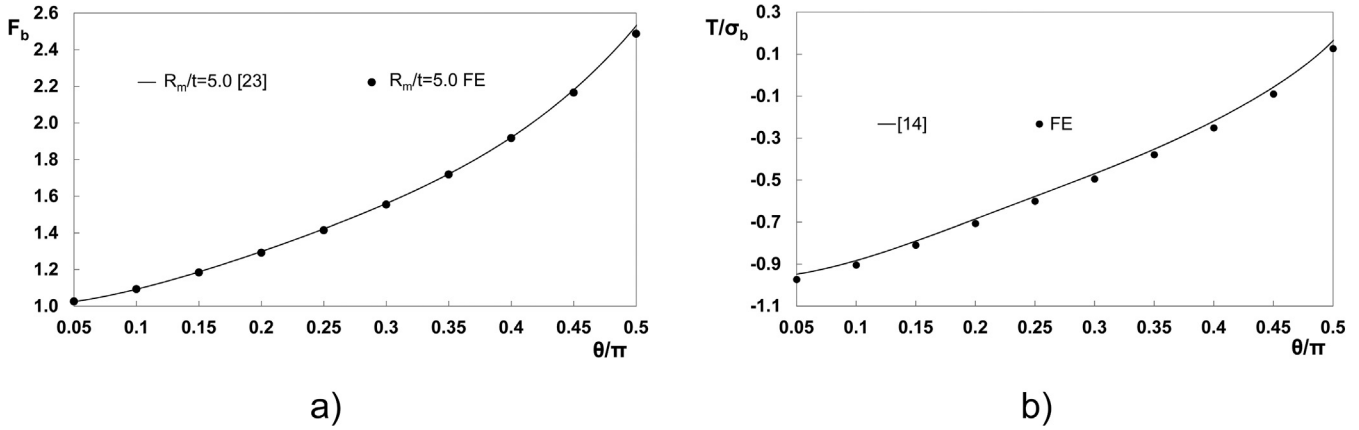


Fig. 8. Comparison of current and literature normalized solutions for a) stress intensity factor with [23] and b) T-stress with [14].

In order to induce pure in-plane bending, rotation was applied to the end of a pipe using the MPC (multi-point constraint) constraint type option within ABAQUS. The end surface of the pipe was constrained by one master node located in the middle of the cross section. Then bending was applied to the master node. This constraint type allows rotation to be transferred from the master node via constrained slave surfaces to the pipe. The MPC option ensures that the rotated end surface remains straight during bending.

Path independence of the extracted values of T does not prove mesh convergence as shown for the SENB specimen in Fig. 4(b). Therefore, mesh convergence studies were performed for pipe models with radius to thickness ratios  $R_m/t = 5, 10$  and  $20$ , by varying the element length along the pipe length, L. The length, L, was fixed as 100 mm and the mean radius as  $R_m = 11$  mm for all cases. It is noted that  $L = 100$  mm was found to be a sufficient length by analyses performed with 150 and 200 mm lengths. Results did not show variation when varying L. Around the semi-circumference of the cylinder, the mesh contained 34 elements resulting in an element size of edge = 1 mm. This number of 34 elements around the semi-circumference was kept constant for all cases. Five steps of mesh refinement were performed for each value of  $R_m/t$  with element size in the length direction in the far-field varying from 10 mm to 1 mm, corresponding to the number of elements varying from 10,000 to 48,000. The number of elements at the focused crack-tip area remained constant (about 5200) for all refinement steps. The finest mesh is shown in Fig. 9.

5.3. Stress intensity factor results

A typical normalized stress intensity factor distribution through the pipe thickness is shown in Fig. 10. A strong reduction in the stress intensity factor is noticeable close to the free surfaces, as was also observed for the SENB geometry, Fig. 5(a).

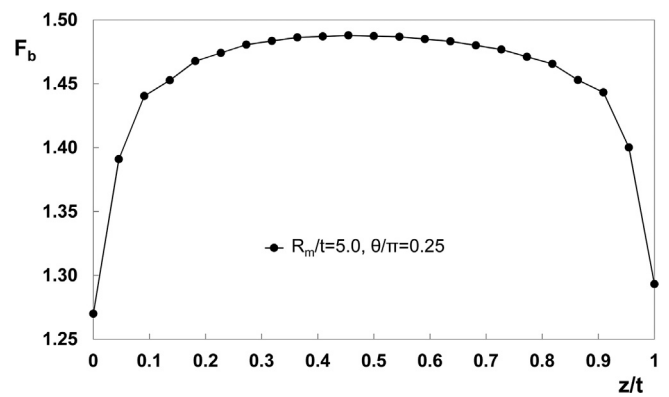


Fig. 10. Typical normalized stress intensity factor  $F_b$  distribution for pipes.

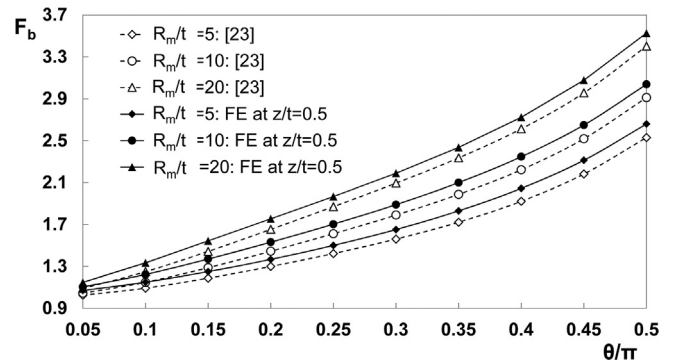


Fig. 11. Comparison of normalized stress intensity factor solutions from the 3D solid finite element model with the solutions from [23].

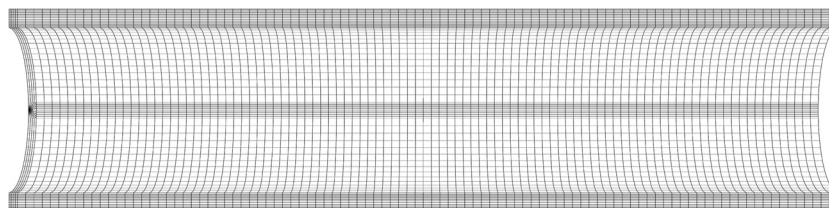


Fig. 9. Mesh for  $R_m/t = 5, \theta/\pi = 0.5$  with the finest mesh with 1 mm element size in the length.

The stress intensity factor distribution along the front of a through-the-thickness crack is significantly influenced by the presence of the 3D vertex singularities. He et al. [27] investigated this phenomenon in cracked plates in mode I loading and concluded that in mode I, the stress intensity factor decreases rapidly near the free surface.

The current study using shell elements has been compared with the stress intensity factor solutions of Lacire et al. [23] in Section 5.1. Similar comparisons with the results from the 3D solid element models are shown in Fig. 11 which contains values of the normalized stress intensity factor,  $F_b$ , at the mean radius,  $R_{12}$ . Solutions for the most refined mesh are given in Fig. 11 but the results were found to be independent of the mesh refinement. It can be seen that higher values of  $R_m/t$  result in higher values of  $F_b$ , while an increase in crack angle  $\theta$  results in higher values of  $F_b$  for all  $R_m/t$ .

A closed form solution has been developed by fitting the finite element results for  $F_b$  at the mean radius by:

$$F_b = f_0 + (\theta/\pi) \left( f_1 + f_2(R_m/t) + f_3(R_m/t)^2 + f_4(R_m/t)^3 + f_5(R_m/t)^4 \right) + (\theta/\pi)^2 \left( f_6 + f_7(R_m/t) + f_8(R_m/t)^2 + f_9(R_m/t)^3 \right) + (R_m/t) \left( f_{10} + f_{11}(R_m/t) + f_{12}(R_m/t)^2 + f_{13}(R_m/t)^3 + f_{14}(R_m/t)^4 \right) \tag{15}$$

where the coefficients  $f_0$  to  $f_{14}$  are given in Table 3. This reproduces the finite element results with high accuracy and is applicable for  $5 \leq R_m/t \leq 20$  and  $\theta/\pi \leq 0.5$ .

The value of  $F_b$  at the mean radius does not provide information on the stress intensity factor distribution through the pipe wall. Therefore, Fig. 12 gives values of  $F_b$  at the positions  $R_5$  and  $R_{19}$ , which are close to the internal and external surfaces of the pipes, respectively. For small cracks, the maximum  $F_b$  values are at  $R_5$  but with increase in crack angle, the location of the maximum  $F_b$

$$T/\sigma_b = t_0 + (\theta/\pi) \left( t_1 + t_2(R_m/t) + t_3(R_m/t)^2 + t_4(R_m/t)^3 + t_5(R_m/t)^4 \right) + (\theta/\pi)^2 \left( t_6 + t_7(R_m/t) + t_8(R_m/t)^2 + t_9(R_m/t)^3 \right) + (R_m/t) \left( t_{10} + t_{11}(R_m/t) + t_{12}(R_m/t)^2 + t_{13}(R_m/t)^3 + t_{14}(R_m/t)^4 \right) \tag{16}$$

changes from  $R_5$  to  $R_{19}$ .

For cleavage fracture, knowledge of the maximum stress intensity factor and its location may be important to accurately predict crack initiation load. For ductile fracture, the average values, which are close to the mid-plane values may be more important. For constraint based failure assessment, the through-wall

distribution of stress intensity factor needs to be combined with the through-wall variation of T-stress, and this is addressed in the next section.

#### 5.4. T-stress results

Results for the normalized T-stress at the mean radius for  $R_m/t = 5$  from the 3D stress element models are shown in Fig. 13. The mesh convergence studies, where the key gives the axial element length in the far field, are included and indicate a strong mesh sensitivity except for small cracks. The results for the two finest meshes are indistinguishable from each other and little different from the solutions with the next finest mesh. Similar mesh sensitivities were found for other  $R_m/t$ . The results from the finest mesh, where axial element length is 1 mm, are therefore taken as converged solutions and presented in Fig. 14. These are normalised by  $\sigma_b$  and compared with the solutions of Lewis and Wang [14] in

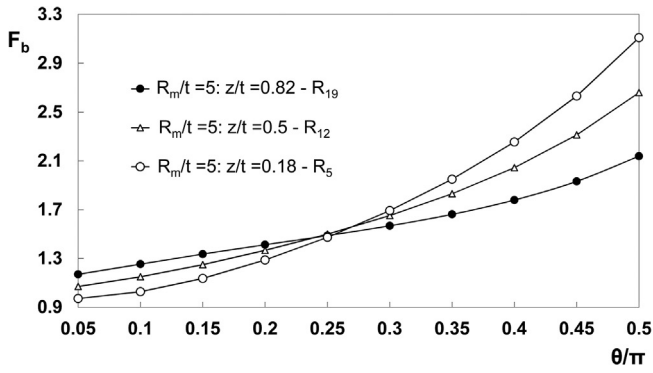
Fig. 14(a) and normalised as  $\beta_T$  in Fig. 14(b). To provide information between  $R_m/t = 10$  and 20, an additional analysis was performed for  $R_m/t = 16.0$  and the results are included in Fig. 14(b).

Unlike the stress intensity factor, it can be seen from Fig. 13 that the T-stress estimate is sensitive to mesh density along the pipe length and this is discussed further in Section 6. The results demonstrate that shell elements are not suitable for T-stress analysis in cracked pipes, although they can estimate the stress intensity factor with reasonable accuracy. Fitting the solid element solutions, including the additional analysis for  $R_m/t = 16.0$  leads to

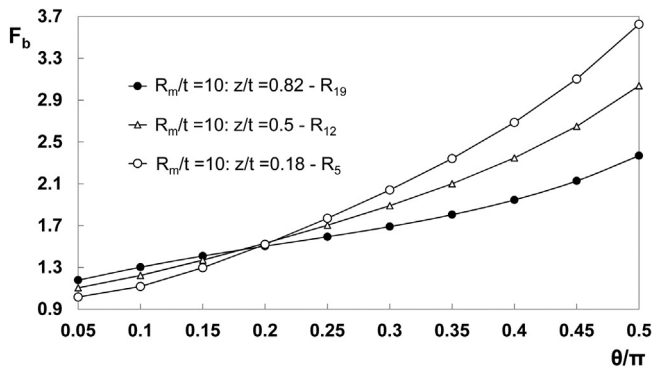
**Table 3**  
Coefficients defining normalised stress intensity factor in Eq. (15).

$f_0$	$f_1$	$f_2$	$f_3$	$f_4$	$f_5$	$f_6$	$f_7$
1.053	-0.00239	0.1919	0.325	-1.13	1.037	-1.86E-05	-0.00141
$f_8$	$f_9$	$f_{10}$	$f_{11}$	$f_{12}$	$f_{13}$	$f_{14}$	
-0.01185	0.01642	-0.8847	12.33	-34.18	54.61	-19.95	

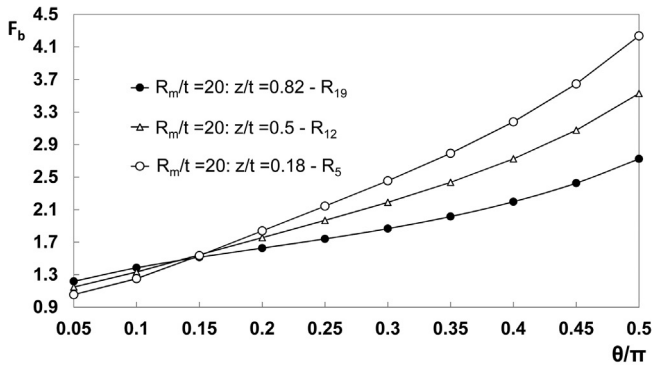
where the coefficients  $t_0$  to  $t_{14}$  are given in Table 4. Eq. (16) reproduces the finite element results with high accuracy and is applicable for  $5 \leq R_m/t \leq 20$  and  $\theta/\pi \leq 0.5$ . Results from Fig. 14(b) obtained using Eqs. (5) and (6) have been fitted by: where the coefficients  $b_0$  to  $b_{14}$  are given in Table 5. This reproduces the finite



a)



b)



c)

Fig. 12. Normalized stress intensity factor  $F_b$  at  $z/t = 0.18$  ( $R_5$ ),  $0.5$  ( $R_{12}$ ) and  $0.82$  ( $R_{19}$ ) for a)  $R_m/t = 5$ , b)  $R_m/t = 10$  and c)  $R_m/t = 20$ .

element results with high accuracy and is applicable for  $5 \leq R_m/t$  and  $t \leq 20$  and  $\theta/\pi \leq 0.5$ .

$$\beta_T = b_0 + (\theta/\pi) \left( b_1 + b_2(R_m/t) + b_3(R_m/t)^2 + b_4(R_m/t)^3 + b_5(R_m/t)^4 \right) + (\theta/\pi)^2 \left( b_6 + b_7(R_m/t) + b_8(R_m/t)^2 + b_9(R_m/t)^3 \right) + (R_m/t) \left( b_{10} + b_{11}(R_m/t) + b_{12}(R_m/t)^2 + b_{13}(R_m/t)^3 + b_{14}(R_m/t)^4 \right)$$

(17)

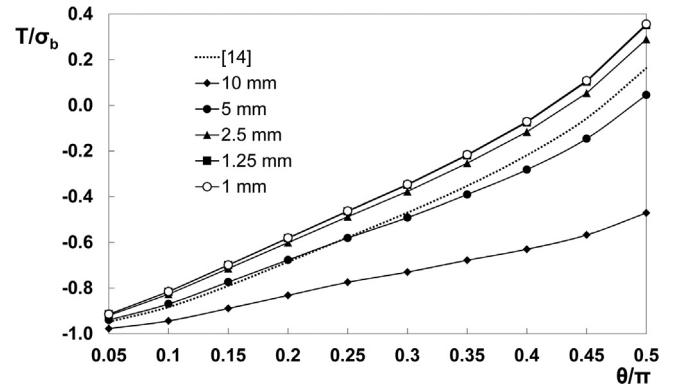


Fig. 13.  $T/\sigma_b$  for various axial element lengths in the far field at  $z/t = 0.5$  for  $R_m/t = 5$ .

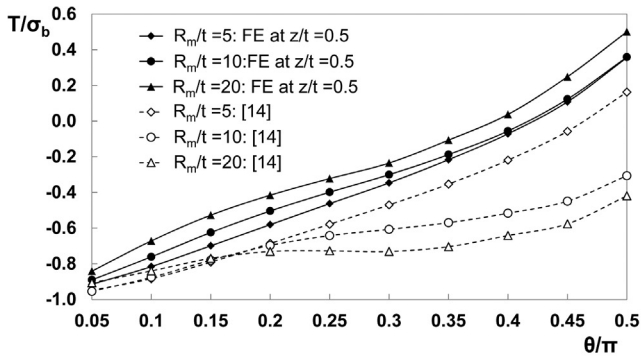
Similar to the stress intensity factor, the T-stress has a strong variation through the thickness. This is shown in Fig. 15. The use of the T-stress distribution through the thickness with the stress intensity factor distribution from Fig. 12 is discussed in Section 6.

6. Discussion

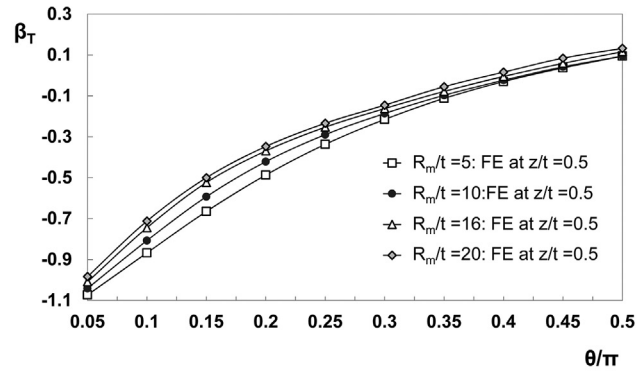
It has been found from the studies of both the SENB specimen and the through-wall cracked pipe using 3D solid elements that the mesh required to obtain converged T-stress solutions needs to be more refined than that required to obtain converged stress intensity factor results. This has been illustrated by the results in Sections 4 and 5 and is further shown in Fig. 16 where convergence with increasing number of finite elements,  $N$ , is plotted. The normalised stress intensity factor, Fig. 16(a), shows rapid convergence compared to that for T-stress, Fig. 16(b).

One possible reason for the difference in convergence is that it was found that the stresses  $\sigma_{xx}$  and  $\sigma_{yy}$  converged from above and below, respectively; therefore, the error in T-stress was essentially twice the error in either stress component, see Eq. (2), and in stress intensity factor. A second reason is that errors in the far field stress distribution parallel to the crack may have little effect on stress intensity factor but have a greater effect on the T-stress, in the same way that biaxial stress affects T-stress directly but not stress intensity factor, for example [28]. Therefore, far field mesh refinement is more important for T-stress calculations than for stress intensity factor calculations. This finding suggests that it is necessary to be cautious in using T-stress solutions in the literature, if these solutions were obtained with a mesh refinement that only guaranteed convergence of the stress intensity factor solutions and no further convergence checks were made.

For selected cases, independent finite element analyses have been performed by the authors and a range of methods for evaluating T-stress have been used to give confidence in the results. In conjunction with the convergence checks and the comparisons with the established plane strain SENB solutions, this gives confidence that the solutions generated and fitted by Eqs. (16) and (17)



a)



b)

Fig. 14. Normalised T-stress at  $z/t = 0.5$  as a function of crack size: a) normalised by  $\sigma_b$  and compared with the solutions of [14]; b) normalised as  $\beta_T$ .

Table 4

Coefficients defining normalised constraint  $T/\sigma_b$  in Eq. (16).

$t_0$	$t_1$	$t_2$	$t_3$	$t_4$	$t_5$	$t_6$	$t_7$
-0.8399	-0.02319	0.6591	-3.084	4.94	-2.599	0.000654	-0.01403
$t_8$	$t_9$	$t_{10}$	$t_{11}$	$t_{12}$	$t_{13}$	$t_{14}$	
0.05401	-0.05076	-3.389	38.22	-114.4	161.2	-77.29	

Table 5

Coefficients defining normalised constraint  $\beta_T$  in Eq. (17).

$b_0$	$b_1$	$b_2$	$b_3$	$b_4$	$b_5$	$b_6$	$b_7$
-1.168	-0.01795	0.6099	-3.155	5.642	-3.294	0.000498	-0.01187
$b_8$	$b_9$	$b_{10}$	$b_{11}$	$b_{12}$	$b_{13}$	$b_{14}$	
0.04901	-0.05297	0.08717	30.89	-110.4	163.8	-93.84	

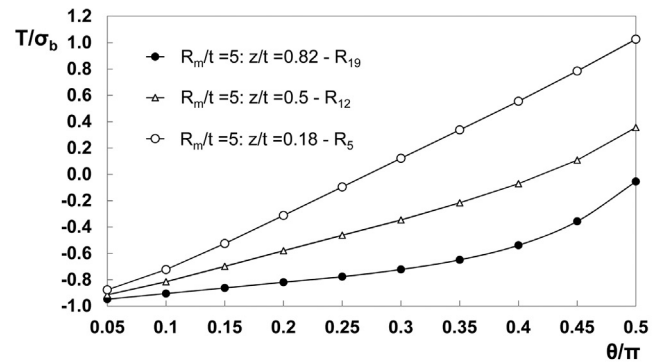
are accurate and suitable for practical use.

It can be seen from Fig. 15 that the greatest loss of constraint is near the outside surface of the pipe and for small cracks. For larger cracks, the T-stress is positive and therefore the conventional high constraint fracture toughness will be relevant to fracture mechanics assessments. The highest stress intensity factor for small through-wall cracks also tends to be at the outside of the pipe, Fig. 12. Therefore, for small cracks the greatest benefit of loss of constraint coincides with the highest stress intensity factor through the thickness. For ductile crack initiation, which is little affected by constraint, this may not be important. However, for cleavage fracture which is more constraint sensitive, this suggests that it may be overly conservative to base fracture assessments simply on the maximum stress intensity factor through the thickness.

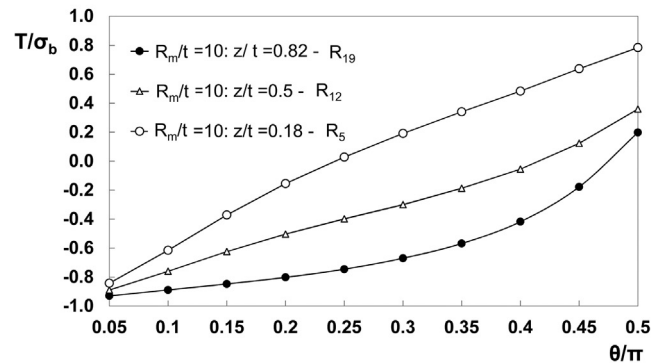
## 7. Conclusions

It has been found that the mesh required to obtain converged T-stress solutions when using 3D solid elements needs to be more refined than that required to obtain converged stress intensity factor results. It has also been found that shell elements are not suitable for T-stress analysis in through-wall cracked pipes, although they can estimate the stress intensity factor within reasonable accuracy.

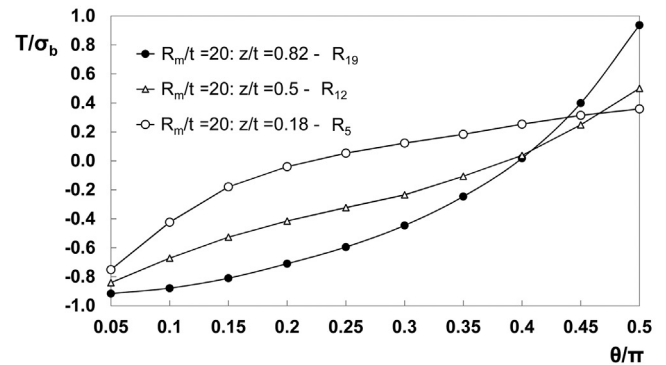
Using refined 3D meshes of solid elements, parametric studies have been performed to generate accurate mid-wall stress intensity factor and T-stress solutions for pipes with through-wall cracks under bending. These have been fitted by polynomial equations



a)



b)



c)

Fig. 15. Normalized T-stress,  $T/\sigma_b$  at  $z/t = 0.18$  (R5),  $0.5$  (R12) and  $0.82$  (R19) for a)  $R_m/t = 5$ , b)  $R_m/t = 10$  and c)  $R_m/t = 20$ .

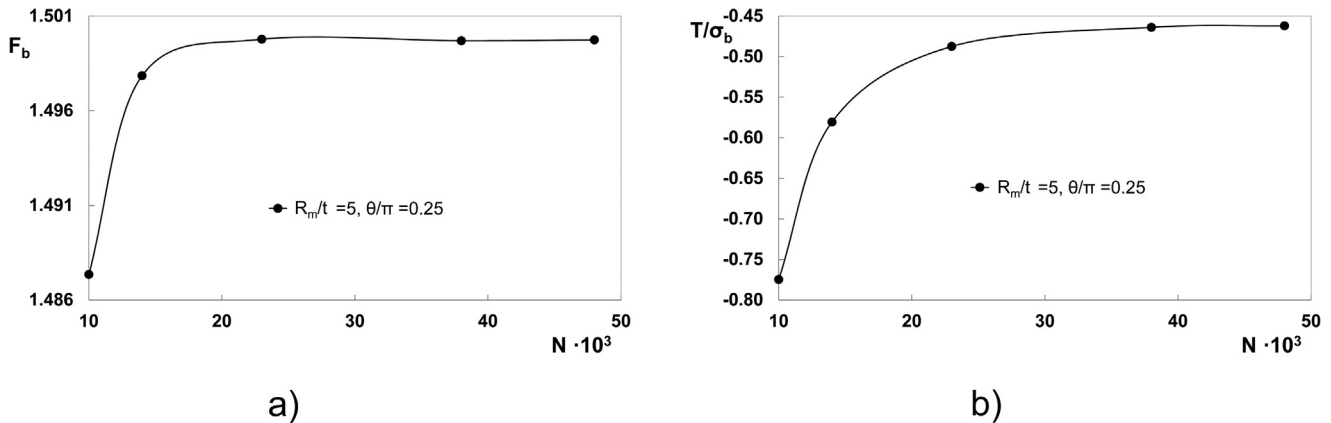


**Fig. 16.** Convergence of results with increasing number of finite elements for pipe with  $R_m/t = 5$  and a through-wall crack of size  $\theta/\pi = 0.25$ : a) normalised stress intensity factor; b) normalised T-stress.

enabling their use for practical assessments for a range of crack sizes and pipe radius to thickness ratio.

In addition to mid-wall values, solutions have also been given for stress intensity factor and T-stress near the inner and outer pipe surfaces to enable more refined constraint based assessments to determine the location of crack initiation.

#### Acknowledgements

Support from the Engineering and Physical Sciences Research Council under grant reference EP/K007815/1 is gratefully acknowledged.

#### References

- [1] Gupta M, Alderliesten RC, Benedictus R. A review of T-stress and its effects in fracture mechanics. *Eng Fract Mech* 2014;134:218–41.
- [2] Sarzosa DFB, Ruggieri C. A numerical investigation of constraint effects in circumferentially cracked pipes and fracture specimens including ductile tearing. *Int J Pres Ves Pip* 2014;120–121:1–18.
- [3] Park S, Yoo SS, Min JK, Koo JM, Seok CS. Evaluation of fracture toughness characteristics for nuclear piping using various types of specimens. *Int J Pres Ves Pip* 2012;90–91:9–16.
- [4] Koo JM, Park S, Seok CS. Evaluation of fracture toughness of nuclear piping using real pipe and tensile compact pipe specimens. *Nucl Eng Des* 2013;259: 198–204.
- [5] Kofiani K, Nonn A, Wierzbicki T. New calibration method for high and low triaxiality and validation on SENT specimens of API X70. *Int J Pres Ves Pip* 2013;111–112:187–201.
- [6] Tan JP, Wang GZ, Xuan FZ, Tu ST. Correlation of creep crack-tip constraint between axially cracked pipelines and test specimens. *Int J Pres Ves Pip* 2012;98:16–25.
- [7] Dadfarnia M, Sofronis P, Somerday BP, Balch DK, Schembri P, Melcher R. On the environmental similitude for fracture in the SENT specimen and a cracked hydrogen gas pipeline. *Eng Fract Mech* 2011;78:2429–38.
- [8] Zhou DW. Measurement and modelling of R-curves for low constraint specimens. *Eng Fract Mech* 2011;78:605–22.
- [9] Nyhus B, Zhang ZL, Thaulow C. Normalisation of material crack resistance curves by the T-stress. In: Proceedings of 14th European conference on fracture, Cracow, Poland; 2002.
- [10] R6: assessment of the integrity of structures containing defects, Revision 4, including subsequent updates. Gloucester, UK: EDF Energy Generation; 2015.
- [11] Huh N-S. Elastic T stress estimates for circumferential surface-cracked cylinders. *Fatigue Fract Eng Mater Struct* 2006;29:57–9.
- [12] Jayadevan KR, Thaulow C, Ostby E, Berg E, Skallerud B, Holthe K, et al. Structural integrity of pipelines: T-stress by line-spring. *Fatigue Fract Eng Mater Struct* 2005;28:467–88.
- [13] Qian X. K<sub>I</sub>-T estimation for embedded flaws in pipes-Part II: circumferentially oriented cracks. *Int J Pres Ves Pip* 2010;87:150–64.
- [14] Lewis T, Wang X. The T-stress solutions for through-wall circumferential cracks in cylinders subjected to general loading conditions. *Eng Fract Mech* 2008;75:3206–25.
- [15] Bonade RA. Constitutive behaviour and fracture properties of tempered martensitic steels for nuclear applications: experimental and modelling. *Ecole Polytech Fed Lausanne* 2006:211.
- [16] Zhao J, Guo W. Three-parameter K-T-T<sub>z</sub> characterization of the crack-tip field in compact-tension-shear specimens. *Eng Fract Mech* 2012;92:72–88.
- [17] Beltz GE, Machova A. Effect of T-stress on dislocation emission in iron. *Scr Mater* 2004;50:483–7.
- [18] Sherry AH, France CC, Goldthorpe MR. Compendium of T-stress solutions for two and three dimensional cracked geometries. *Fatigue Fract Eng Mater Struct* 1995;18(1):141–55.
- [19] Meliani MH, Azari Z, Pluvinage G, Matvienko YG. The effective T-stress estimation and cracks emanating from U-notches. *Eng Fract Mech* 2010;77: 1682–92.
- [20] Shlyannikov VN, Boychenko NV, Tumanov AV, Fernández-Canteli A. The elastic and plastic constraint parameters for three-dimensional problems. *Eng Fract Mech* 2014;127:83–96.
- [21] Moustabchir H, Azari Z, Hariri S, Dmytrakh I. Experimental and computed stress distribution ahead of a notch in a pressure vessel: application of T-stress concept. *Comp Mater Sci* 2012;58:59–66.
- [22] Lei Y, Li Y, Gao Z. Global limit load solutions for thick-walled cylinders with circumferential cracks under combined internal pressure, axial force and bending moment, Part I: theoretical solutions. *Int J Pres Ves Pip* 2014;114–115:23–40.
- [23] Lacire MH, Chapuliot S, Marie S. Stress intensity factors of through wall cracks in plates and tubes with circumferential cracks. *ASME PVP* 1999;388:13–21.
- [24] ABAQUS Standard/User's manual. Version 6.11.1. Dassaults Systemes Inc; 2011.
- [25] Nakamura T, Parks DM. Determination of elastic T-stress along three-dimensional crack fronts using an interaction integral. *Int J Solid Struct* 1992;29:1597–611.
- [26] Lu K, Meshii T. Three-dimensional T-stress for three-point-bend specimens with large thickness variation. *Eng Fract Mech* 2014;116:197–203.
- [27] He Z, Kotusov A, Berto F. Effect of vertex singularities on stress intensities near plate free surfaces. *Fatigue Fract Eng Mater Struct* 2015;38:860–9.
- [28] Meek C, Ainsworth RA. The effects of load biaxiality and plate length on the limit load of a centre cracked plate. *Eng Fract Mech* 2015;147:306–17.

## Update

# International Journal of Pressure Vessels and Piping

Volume 168, Issue , December 2018, Page 335

DOI: <https://doi.org/10.1016/j.ijpvp.2018.07.003>



## Corrigendum

## Corrigendum to “T-stress solutions for through-wall circumferential cracks in straight pipes under bending” [Int. J. Pres. Ves. Piping 152 (2017) 27–37]

M. Gintalas<sup>1,\*</sup>, R.A. Ainsworth<sup>2</sup>, F. Scenini<sup>3</sup><sup>1</sup> The University of Cambridge, Department of Materials Science and Metallurgy, Maxwell Centre, JJ Thomson Ave, Cambridge, CB3 0HE, UK<sup>2</sup> The University of Manchester, School of Mechanical, Aerospace and Civil Engineering, Pariser Building, Sackville Street, Manchester, M13 9PL, UK<sup>3</sup> The University of Manchester, School of Materials, Sackville Street, Manchester, M13 9PL, UK

The authors regret.

In equations (15), (16) and (17) the variable  $R_m/t$  should be replaced by  $\theta/\pi$  and the variable  $\theta/\pi$  should be replaced by  $R_m/t$ . The corrected versions of the equations are:

$$F_b = f_0 + (R_m/t)(f_1 + f_2(\theta/\pi) + f_3(\theta/\pi)^2 + f_4(\theta/\pi)^3 + f_5(\theta/\pi)^4) \\ + (R_m/t)^2(f_6 + f_7(\theta/\pi) + f_8(\theta/\pi)^2 + f_9(\theta/\pi)^3) \\ + (\theta/\pi)(f_{10} + f_{11}(\theta/\pi) + f_{12}(\theta/\pi)^2 + f_{13}(\theta/\pi)^3 + f_{14}(\theta/\pi)^4) \quad (15)$$

$$T/\sigma_b = t_0 + (R_m/t)(t_1 + t_2(\theta/\pi) + t_3(\theta/\pi)^2 + t_4(\theta/\pi)^3 + t_5(\theta/\pi)^4) \\ + (R_m/t)^2(t_6 + t_7(\theta/\pi) + t_8(\theta/\pi)^2 + t_9(\theta/\pi)^3) \\ + (\theta/\pi)(t_{10} + t_{11}(\theta/\pi) + t_{12}(\theta/\pi)^2 + t_{13}(\theta/\pi)^3 + t_{14}(\theta/\pi)^4) \quad (16)$$

$$\beta_T = b_0 + (R_m/t)(b_1 + b_2(\theta/\pi) + b_3(\theta/\pi)^2 + b_4(\theta/\pi)^3 + b_5(\theta/\pi)^4) \\ + (R_m/t)^2(b_6 + b_7(\theta/\pi) + b_8(\theta/\pi)^2 + b_9(\theta/\pi)^3) \\ + (\theta/\pi)(b_{10} + b_{11}(\theta/\pi) + b_{12}(\theta/\pi)^2 + b_{13}(\theta/\pi)^3 + b_{14}(\theta/\pi)^4) \quad (17)$$

The authors would like to apologise for any inconvenience caused.

DOI of original article: <https://doi.org/10.1016/j.ijpvp.2017.04.004>

\* Corresponding author.

E-mail address: [mg793@cam.ac.uk](mailto:mg793@cam.ac.uk) (M. Gintalas).<https://doi.org/10.1016/j.ijpvp.2018.07.003>

Available online 21 July 2018

0308-0161/ © 2018 Published by Elsevier Ltd.